

---

---

# Patient-Specific Radiation Dosimetry of $^{99m}\text{Tc}$ -HYNIC-Tyr<sup>3</sup>-Octreotide in Neuroendocrine Tumors

Joshua Grimes<sup>1,2</sup>, Anna Celler<sup>1,2</sup>, Bozena Birkenfeld<sup>3</sup>, Sergey Shcherbinin<sup>2</sup>, Maria H. Listewnik<sup>3</sup>, Hanna Piwowska-Bilska<sup>3</sup>, Renata Mikołajczak<sup>4</sup>, and Piotr Zorga<sup>3</sup>

<sup>1</sup>Department of Physics and Astronomy, University of British Columbia, Vancouver, British Columbia, Canada; <sup>2</sup>Department of Radiology, University of British Columbia, Vancouver, British Columbia, Canada; <sup>3</sup>Nuclear Medicine Department, Pomeranian Medical University, Szczecin, Poland; and <sup>4</sup>IAE POLATOM Radioisotope Centre, Warsaw, Poland

---

$^{99m}\text{Tc}$ -hydrazinonicotinamide-Tyr<sup>3</sup>-octreotide ( $^{99m}\text{Tc}$ -HYNIC-TOC) is increasingly gaining acceptance as a new radiopharmaceutical for the diagnosis of pathologic lesions overexpressing somatostatin receptors. However, little information has been published about the radiation dosimetry of this agent. The aim of this study was to assess the biodistribution and radiation dosimetry of commercially available  $^{99m}\text{Tc}$ -HYNIC-TOC. A dose calculation procedure designed to be feasible to implement in a busy clinical environment was used. **Methods:** Twenty-eight patients were imaged for suspected neuroendocrine tumors using a series of whole-body planar, dynamic planar, and SPECT/CT studies, after injection with  $^{99m}\text{Tc}$ -HYNIC-TOC. Patient-specific dosimetry was performed using the OLINDA/EXM software with time-integrated activity coefficients estimated from a hybrid planar/SPECT technique. A phantom experiment was performed to establish adaptive thresholds for determination of source region volumes and activities. **Results:** Pathologic uptake, diagnosed as due to neuroendocrine tumors, was observed in 12 patients. Normal organs with significant uptake included the kidneys, liver, and spleen. The mean effective dose after  $^{99m}\text{Tc}$ -HYNIC-TOC injection was  $4.6 \pm 1.1$  mSv. Average normal-organ doses were  $0.030 \pm 0.012$ ,  $0.021 \pm 0.007$ , and  $0.012 \pm 0.005$  mGy/MBq for the spleen, kidneys, and liver, respectively. The interpatient kidney dose ranged from 0.011 to 0.039 mGy/MBq, whereas the range of tumor doses varied from 0.003 to 0.053 mGy/MBq. The ratio of tumor to kidney dose ranged from 0.13 to 2.9. The optimal thresholds for recovery of true activity in the phantom study were significantly lower than those used for volume determination.

**Conclusion:** The patient-specific 3-dimensional dosimetry protocol used in this study is a clinically feasible technique that has been applied to demonstrate large dose variations in tumors and normal organs between patients imaged with  $^{99m}\text{Tc}$ -HYNIC-TOC.

**Key Words:** SPECT/CT;  $^{99m}\text{Tc}$ -HYNIC-Tyr<sup>3</sup>-octreotide; neuroendocrine tumors; somatostatin receptor imaging; patient-specific dosimetry

**J Nucl Med 2011; 52:1474–1481**  
DOI: 10.2967/jnumed.111.088203

Neuroendocrine tumors represent a group of human tumors known to express somatostatin receptors to a varying degree (1). Accordingly, somatostatin receptor imaging with a radiolabeled somatostatin analog is an important diagnostic procedure that is routinely used for localization of primary and metastatic sites of disease, staging, qualification of patients for treatment with cold or radiolabeled somatostatin analog, and therapy follow-up. Until recently, the radiopharmaceutical of choice for neuroendocrine tumor imaging was  $^{111}\text{In}$ -diethylenetriaminepentaacetic acid (DTPA)-octreotide (OctreoScan; Mallinckrodt Inc.) (2). However, there are drawbacks to imaging with  $^{111}\text{In}$ , given its high cost and emission of medium-energy photons, which result in suboptimal image quality and elevated radiation dose to the patient and staff.

As an alternative to  $^{111}\text{In}$ , a  $^{99m}\text{Tc}$ -labeled somatostatin analog,  $^{99m}\text{Tc}$ -hydrazinonicotinamide-Tyr<sup>3</sup>-octreotide ( $^{99m}\text{Tc}$ -HYNIC-TOC), has been used by several groups for early diagnosis and staging of tumors expressing somatostatin receptors (3–5) and has been demonstrated to provide improved neuroendocrine tumor lesion detection, compared with other imaging agents such as  $^{111}\text{In}$ -DTPA-octreotide (6). PET tracers such as  $^{68}\text{Ga}$ -labeled DOTA derivatives of somatostatin have also become popular in recent years (7–9). However, application of these tracers is limited to PET centers, whereas SPECT still remains the most prevalent nuclear medicine imaging modality worldwide.

Given the promising applications of  $^{99m}\text{Tc}$ -HYNIC-TOC, there are situations in which accurate quantification of activity and estimation of dose is desirable. In particular, tumor and organ uptake is indicative of the intensity of tumor somatostatin receptor expression and potential organ toxicities, which can influence treatment planning decisions. However, little has been published about the radiation dosimetry of  $^{99m}\text{Tc}$ -HYNIC-TOC. To the best of our knowledge, the only paper addressing this issue was published by González-Vázquez et al., who used a 2-dimensional (2D) dosimetry protocol based on a series of conjugate-view whole-body scans for dose estimation (10).

---

Received Jan. 21, 2011; revision accepted Apr. 21, 2011.  
For correspondence or reprints contact: Joshua Grimes, Department of Physics and Astronomy, University of British Columbia, 366-828 W. 10th Ave., Vancouver, BC V5Z 1M9, Canada.  
E-mail: grimes@physics.ubc.ca  
Published online Jul. 27, 2011.  
COPYRIGHT © 2011 by the Society of Nuclear Medicine, Inc.

The aim of this paper is to present a 3-dimensional (3D) image-based dose calculation method that we used for the dosimetry and biodistribution analysis of commercially available  $^{99m}\text{Tc}$ -HYNIC-TOC ( $^{99m}\text{Tc}$ -Tektrotyd; IAE POLATOM) in a group of 28 patients with diagnosed or suspected neuroendocrine tumors. The procedure used a hybrid planar/SPECT technique (11) to determine source region cumulated activities, and adaptive thresholds based on the source-to-background ratio (SBR) of activities were used for tumor and organ segmentation (12). This technique was chosen because it would be practical to implement in a busy clinical environment without compromising the accuracy of dose determination.

## MATERIALS AND METHODS

### Patient Studies

Twenty-eight patients (14 men and 14 women) with diagnosed or suspected neuroendocrine tumors and a median age of 54 y (range 23–78 y) were included in this study, which was approved by the Ethics Review Board at our institution (Pomeranian Medical University). All scans were acquired using a dual-head Infinia Hawkeye 4 camera (GE Healthcare). For each patient, multiple (3–4) whole-body planar scans and a single SPECT/CT scan were obtained over a period of 1–24 h after injection of 750–1,020 MBq of  $^{99m}\text{Tc}$ -HYNIC-TOC. The whole-body anterior and posterior views were acquired into  $256 \times 1,024$  matrices with a pixel size of 2.21 mm and a scan speed of 20 cm/min. For quality control, in all planar studies a small  $^{99m}\text{Tc}$  point source was placed beside the patient within the field of view of the camera. For the SPECT scans, 60 projections were acquired over  $360^\circ$  with a noncircular orbit. All SPECT scans used  $128 \times 128$  projection matrices with a pixel size of 4.42 mm and 20 s per stop. The low-dose CT component (Hawkeye) was used to create attenuation maps and, in a few cases, to determine organ boundaries.

Additionally, for 19 patients, a 30-min dynamic planar scan was obtained to investigate the temporal characteristics of the early uptake phase. Each dynamic scan began immediately after the injection and recorded 60 frames for 30 s per frame into  $128 \times 128$  matrices for anterior and posterior views of the suspected tumor location.

In all patients, this  $^{99m}\text{Tc}$ -HYNIC-TOC study was performed as a part of the diagnostic routine for primary and metastatic lesion localization, staging, or follow-up. The final diagnosis of these patients was based on histopathologic examination.

### Phantom Experiment

In preparation for use of adaptive thresholds based on the SBR for tumor and organ segmentation in the patient studies, a phantom experiment was performed. This experiment was used to generate plots of optimal threshold versus SBR based on known object volumes and activities in the phantom. For this purpose, 8 cylindrical plastic bottles, four 33 mL and four 120 mL in volume, were filled with  $^{99m}\text{Tc}$  activity of concentrations ranging from 20 to 80 kBq/mL. The bottles were placed inside 2 large cylinders, each with a volume of about 7,000 mL (Jaszczak phantoms) and an initial background activity concentration of 8 kBq/mL. The 2 large cylindrical phantoms containing the bottles were scanned by SPECT/CT simultaneously by placing them upright beside each other on the bed so that both could be included in a single SPECT field of view. Next, the background activity was increased to 11 kBq/mL in one of the phantoms,

for which the SPECT/CT scan was repeated. Acquisition parameters for both SPECT scans of the phantoms were identical to those used in patient studies.

### Determination of Time–Activity Curves and Effective Half-Lives

The first step in data processing for the hybrid planar/SPECT procedure is determination of the shape of the time–activity curves for tumors and normal organs from the whole-body images. The first image from the series of whole-body scans of each patient was selected, and oversized regions were manually drawn around every tumor and organ with significant uptake, which included the kidneys, liver, spleen, and to a lesser extent thyroid. Each region contained the tumor or organ and the surrounding background, and care was taken to avoid other nearby areas with high uptake. In patients with liver metastases, regions were drawn around only the whole liver, and the individual metastases were not included in this analysis. Regions of interest (ROIs) were automatically created by applying a threshold of 50% of the maximum pixel counts. These 2D ROIs were then manually registered (by translation) to the data from corresponding regions in the remaining whole-body scans at subsequent time points. In addition to this procedure for segmenting individual organs and tumors by thresholding, regions were manually drawn around the whole body.

For each ROI segmented from the planar data, adjacent background regions were drawn in order to perform geometrically based background subtraction (13) using the background correction factor,  $F$ :

$$F = \{[1 - t_{BG} \cdot (I_{BG}/I_A)][1 - t_{BG} \cdot (I_{BG}/I_P)]\}^{1/2}, \quad \text{Eq. 1}$$

where  $I_A$  and  $I_P$  represent the counts in the anterior and posterior views of the source ROI,  $I_{BG}$  is the mean counts per pixel in the background region multiplied by the number of pixels in the source ROI, and  $t_{BG}$  is the fraction of the patient thickness corresponding to background tissue at the location of the ROI. Patient and source region thicknesses were estimated from the SPECT image. In most cases, the product of the background correction factor and the geometric mean of counts,  $F(I_A I_P)^{1/2}$ , was plotted versus time. In some instances, tumors were found near the surface and appeared in only 1 planar view, in which case only counts from that single view were used. No attenuation correction was performed for the planar studies because the attenuation correction factor should remain constant at each time point, and these data were used only for determining the shape of the time–activity curves. For each source region, a monoexponential fit through the planar data was used to find the effective decay constant,  $\lambda_{eff}$  which is a combination of the decay constants corresponding to physical decay and biologic removal. Using the quantitative SPECT images, we subsequently normalized these monoexponential fits to pass through the data point corresponding to the reconstructed SPECT activity ( $A_{SPECT}$ ) at the time of the SPECT acquisition ( $t_{SPECT}$ ). The resulting activity as a function of time,  $A(t)$ , for each source region could then be expressed as:

$$A(t) = A_{SPECT} e^{-\lambda_{eff}(t - t_{SPECT})}, \quad \text{Eq. 2}$$

Additionally, to explore the error in time-integrated activity estimates associated with this monoexponential fit to the data, for 20 patients biexponential functions were fit to the spleen, where uptake was observed to be slower than in the other organs.

The fitted values for the decay constants were used to determine the effective half-life in each source ROI using  $T_{eff} = \ln(2)/\lambda_{eff}$ . To verify our procedure, ROIs were also drawn surrounding the  $^{99m}\text{Tc}$  markers placed outside the patient. The calculated half-life obtained from the exponential fit through the geometric mean of the counts in these ROIs plotted versus time was investigated to confirm that it matched the physical half-life of  $^{99m}\text{Tc}$  (6.01 h).

### SPECT Reconstruction

All patient and phantom SPECT reconstructions were performed using our quantitative qSPECT method (14), which is based on the iterative ordered-subsets expectation maximization algorithm. In all cases, the reconstruction used 6 iterations and 10 subsets and included resolution recovery and CT-based attenuation and analytic scatter corrections (15,16). A calibration experiment was performed to determine the sensitivity of the camera (in cpm/kBq) so that counts in the reconstructed images could be translated into absolute activity. This calibration experiment involved a 5-min planar scan of a point source of known activity determined in a well counter, placed in air about 20 cm away from the surface of each of the 2 detectors.

### Adaptive Threshold Determination

For the phantom study, background activity concentrations were measured from the reconstructed SPECT images inside volumes of interest manually delineated in the areas outside the bottles. The maximum activity in the image of each bottle was defined as the average activity in the 9 hottest voxels. To determine the value of the threshold that would correspond to the true volume of each bottle, different thresholds computed as percentages of the maximum activity were applied until the optimal threshold that returned the bottle's true volume (ThV) was found. The optimal thresholds were plotted versus SBR and fitted with an inverse function ( $\text{ThV} = a_1 + b_1/\text{SBR}$ ). The same procedure was repeated, this time to determine the optimal threshold necessary to recover each bottle's true activity (ThA). An inverse function was used again to fit results from this second dataset ( $\text{ThA} = a_2 + b_2/\text{SBR}$ ).

To verify the relationships found for ThV and ThA, adaptive thresholds calculated using the fitted parameters were applied in the analysis of the images from a separate phantom experiment comprising 3 bottles, 33 mL in volume, filled with  $^{99m}\text{Tc}$  activity placed in active water. The delineated volumes and activities of these bottles were compared with the known true values.

### Activity Quantification and Dose Estimation for Patient Data

Volumes and absolute activities of tumors and other organs were obtained from the reconstructed SPECT images using 3 different thresholding techniques. These activity values were used for rescaling the time-activity curves obtained from processing the planar data.

For each patient, tumors and organs were separated in 3D by manual drawing of regions in each transaxial or coronal slice of the SPECT image. Similar to the method used in processing the planar data, these regions included the source and some of the surrounding background activity. To define tumor and organ volumes inside these regions, ThV, the adaptive threshold as established by the phantom study for recovery of the true volume, was applied. Tumor and organ activities were found using ThA, the adaptive threshold determined from the phantom study for recovery of the true activity. Because the values of ThV and ThA depend on the SBR, these thresholds were applied only after the

patient-specific SBRs for each tumor and organ had been determined. An estimate of the source region activity concentration after segmentation with a 40% threshold and a background activity concentration from regions manually delineated outside the tumor or organ under investigation were used for this purpose. The choice of a fixed 40% threshold was based on the fact that this value is already commonly used in clinical practice (17). The approximate SBRs were then applied to get the values of ThV and ThA using the relationships obtained in the phantom study.

Regions segmented by use of ThV provided volume estimates and thus patient-specific organ masses. Tumor and organ absolute activities that were determined from the SPECT images using ThA provided the normalization factors on which rescaling of the time-activity curves for each patient was based. Source region time-integrated activity coefficients (TIACs) (formerly called residence times (18)) were then computed by integrating the time-activity curves and dividing the obtained values by the injected activities. In addition, the TIAC for the urinary bladder contents was calculated using the voiding bladder model. Inputs for the voiding bladder model, which include the fractions and biologic half-lives for activity excreted in the urine, were obtained from the whole-body clearance curves. The TIAC for the remainder of the body was determined by subtraction of the TIACs calculated for all segmented organs from that of the whole body. Individual tumor and organ doses were then calculated with the OLINDA/EXM 1.1 software (19), using the determined TIACs as input. The organ doses were corrected using the option in OLINDA/EXM to adjust the organ masses to the patient-specific values. Tumor doses were estimated using the sphere model provided by OLINDA/EXM.

## RESULTS

### Time-Activity Curves

Tumors were revealed in 12 of the patients examined in this study. Example whole-body images from 3 of these patients, as well as the image from 1 patient with no visible lesions, are displayed in Figure 1. Patient information, including age, sex, and disease description, is provided in Supplemental Table 1 (supplemental materials are available online only at <http://jnm.snmjournals.org>).

Figure 2 shows typical organ time-activity curves for the left kidney, liver, and spleen in 5 patients. Median values for the effective and biologic half-lives, determined from the exponential fits through the time-activity data for both tumors and organs, are summarized in Table 1. In several instances, most notably for tumors and the spleen of some patients, the time-activity data were more appropriately fit by a biexponential function than by a monoexponential function. The reason for this behavior may be seen when the dynamic data acquired over the first 30 min after injection are analyzed.

The typical uptake behavior in a patient with no visible lesions, as determined by the 30-min dynamic planar scans, is depicted in Figure 3A. In general, the kidneys were found to reach maximum uptake after 5–10 min, followed by the washout phase. In the liver, maximum uptake occurred in less than 5 min, followed by a rapid decrease and then a more gradual washout phase. Uptake in the spleen was slower and usually extended beyond the 30-min scan,

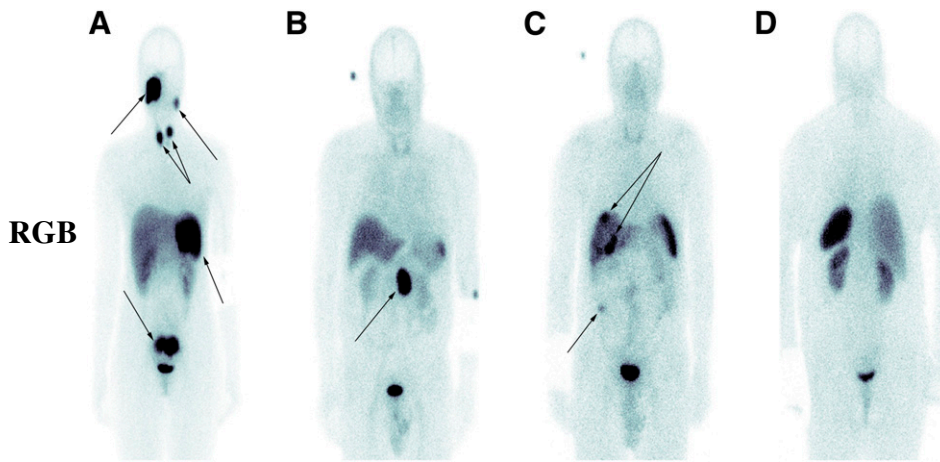


**FIGURE 1.** Anterior whole-body planar images acquired at approximately 1.5 h after injection, with pathologic uptake indicated by arrows. (A) Neuroendocrine tumor in right maxilla with metastasis to left mastoid, both thyroid lobes, left subdiaphragmatic region, and lower intraabdominal region (patient 1). (B) Neuroendocrine tumor in small bowel (patient 24). (C) Neuroendocrine tumor in small bowel with metastasis to liver (patient 28). (D) Example of patient with no visible lesions (patient 5). Posterior view is displayed to clearly show kidney uptake.

explaining why the spleen time–activity curve is better fit by a biexponential function. Figure 3B shows an example of the typical dynamic behavior in a patient, including normal-organ and tumor data. Similar to the spleen, uptake in the tumor increased slowly and did not reach a maximum until after the 30-min scan.

In the comparison of spleen TIACs calculated from time–activity curves fitted by monoexponential and biexponential functions in 20 patients, the monoexponential fit was found to overestimate the biexponentially derived TIACs by  $6.6\% \pm 2.9\%$  on average.

#### Phantom Study

Plots of the thresholds corresponding to the true bottle volume and true activity versus the SBR are shown in Figure 4. Regression analysis of the true-volume threshold data resulted in the expression  $\text{ThV} = 29 + 37.6/\text{SBR}$  ( $R^2 = 0.90$ ). Total activity inside regions delineated using ThV were found to underestimate the true total activity by  $16.8\% \pm 4.3\%$  on average. For the true-activity threshold data, the fitted relationship was evaluated to be  $\text{ThA} = 11.2 + 66.1/\text{SBR}$  ( $R^2 = 0.92$ ).

In the phantom experiment used for validation of these expressions, the average percentage difference between the true bottle volumes and the bottle volumes resulting from use of ThV (defined as  $100\% \times [\text{ThV volume} - \text{true volume}] / \text{true volume}$ ) was  $-6.4\% \pm 1.9\%$ . Using ThA, the average percentage difference between the true bottle activities and the estimated activities was  $-9.6\% \pm 3.3\%$ .

#### Organ Delineation

Delineation of organs in the SPECT images using ThV, evaluated from measured SBRs in each patient and parameters from the phantom study, led to the determination of patient-specific organ masses (Supplemental Table 2). Regions defined using a fixed threshold of 40% underestimated organ volumes obtained using ThV by 22.6% for the kidneys, 11.7% for the liver, and 16.1% for the spleen. A visual check of the SPECT-derived organ contours drawn on the CT slices confirmed that organ segmentation using ThV represented organ boundaries more accurately than the 40% threshold (Fig. 5). Similar to the phantom study, the total activity inside volumes delineated using ThV were lower than the total activity inside volumes delineated using ThA, by 17% on average. Because there is no way to measure true organ activities in patient studies, evaluation of the accuracy of ThA can be based only on phantom experiments.

#### Absorbed Dose Calculation

Table 2 lists the average values of the TIACs used as input for dose calculation with the OLINDA/EXM software. The average relative absorbed doses calculated for normal organs are summarized in Table 3. The spleen typically received the highest relative absorbed dose from the injection of  $^{99\text{m}}\text{Tc}$ -HYNIC-TOC, with an average over all patients of  $0.030 \pm 0.012$  mGy/MBq. The kidneys followed, with an average dose of  $0.021 \pm 0.007$  mGy/MBq, whereas the average doses to the urinary bladder wall, liver,

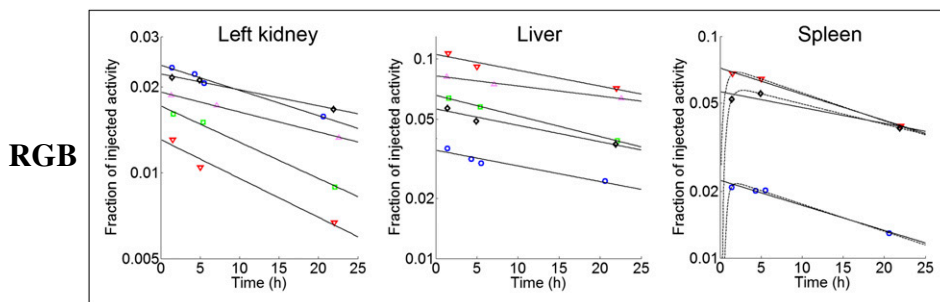


**FIGURE 2.** Examples of kidney and liver decay-corrected time–activity data fitted with monoexponential function for 5 patients. Spleen time–activity data are plotted for 3 of these patients, also showing use of biexponential in addition to monoexponential fit.

**TABLE 1**  
Effective and Biologic Half-Lives Determined from Monoexponential Fits Through Tumors and Normal Organs

Region	Effective half-life (h)	Biologic half-life (h)
Kidneys	5.4 (4.5–5.9)	51.5 (18.6–511.5)
Liver	5.4 (4.6–5.8)	51.0 (20.2–136.0)
Spleen	5.3 (4.9–5.9)	47.6 (27.8–333.5)
Thyroid	4.6 (4.0–4.9)	19.7 (11.9–26.0)
Tumors	5.3 (4.8–6.0)	47.9 (24.1–1,800)

Data are median, followed by range in parentheses.

and thyroid were  $0.014 \pm 0.004$ ,  $0.012 \pm 0.005$ , and  $0.004 \pm 0.001$  mGy/MBq, respectively. The calculated effective doses after  $^{99m}\text{Tc}$ -HYNIC-TOC injection ranged from 2.7 to 6.4 mSv. Average normal-organ doses were also calculated separately for patients with observed pathologic uptake and for those without. A *t* test with a confidence level of 95% showed no statistical difference between the mean doses in any 1 organ in the 2 groups of patients.

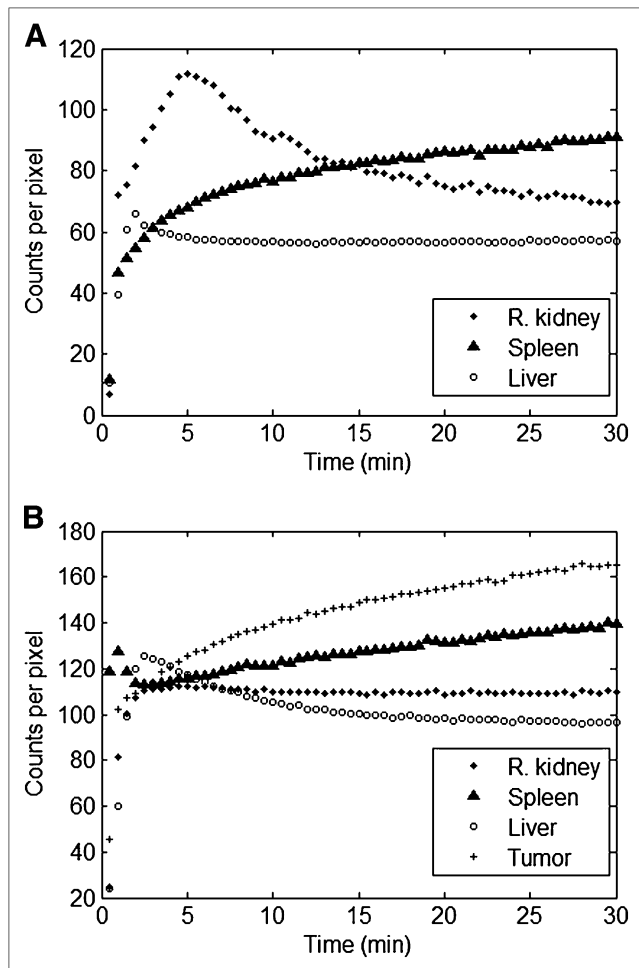


**FIGURE 3.** Dynamic planar plots for patient with no visible lesions (A) and patient with pathologic uptake (B).

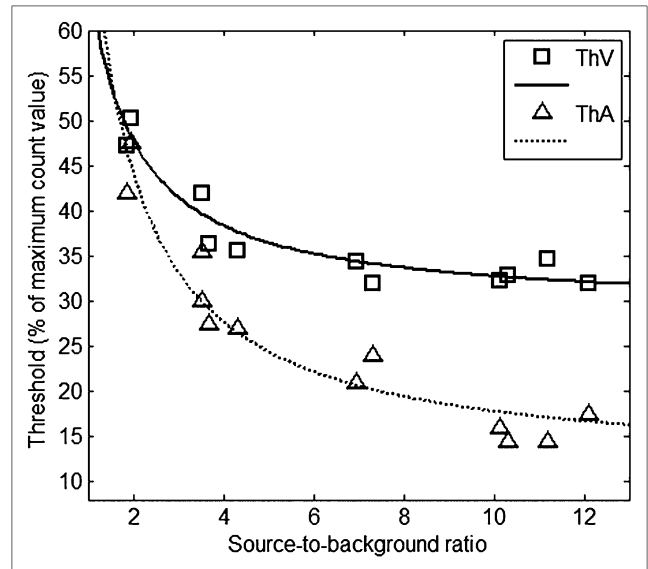


**FIGURE 4.** Adaptive thresholds for determining true bottle volume and true activity as function of SBR, obtained from phantom experiment. ThV and ThA are thresholds used to determine volume and activity, respectively.

The estimated tumor masses and doses along with the normal-organ doses for patients with pathologic uptake are summarized in Table 4. There was a wide spread in tumor relative absorbed dose estimates, ranging from 0.003 to 0.053 mGy/MBq, with most tumor doses at the low end of this range. The median tumor dose was 0.010 mGy/MBq.

### DISCUSSION

The image-based dose calculation method presented in this study was designed to provide accurate patient-specific

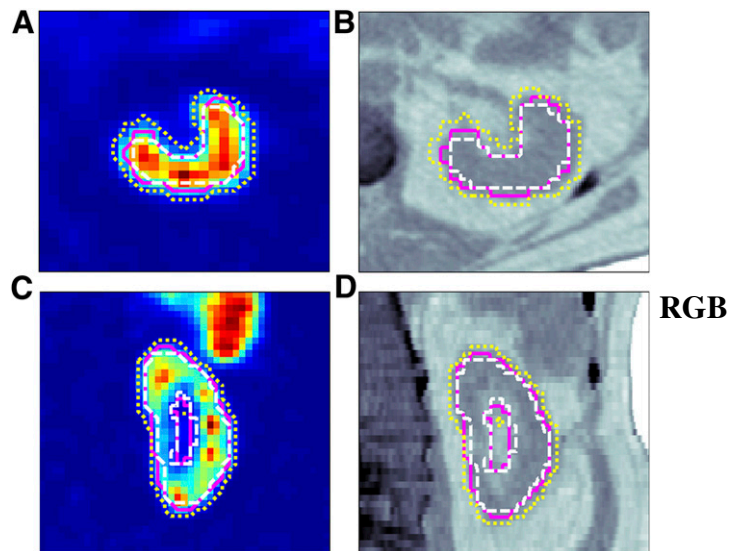


**FIGURE 5.** Delineation of left kidney on transaxial SPECT (A) and CT (B) and coronal SPECT (C) and CT (D), comparing use of fixed 40% threshold (white dashed line), ThV (solid magenta line), and ThA (dotted yellow line).

**TABLE 2**  
Organ TIACs

Organ	TIAC (Bq-h/Bq)
Kidneys	0.35 ± 0.10 (0.19–0.54)
Liver	0.75 ± 0.31 (0.20–1.72)
Spleen	0.43 ± 0.20 (0.04–0.89)
Thyroid	0.01 ± 0.004 (0.01–0.02)
Urinary bladder	0.23 ± 0.09 (0.12–0.53)
Remainder of body	4.34 ± 0.74 (3.00–6.10)

Data are average ± SD, followed by range in parentheses.

dose estimates while working within the limitations of a busy clinical environment. To this end, a hybrid planar/SPECT technique was used to obtain source region cumulated activities, with image segmentation performed using adaptive thresholds.

The fitted parameters for ThV resulted in lower thresholds than what has previously been reported by investigators using the adaptive threshold approach. This disparity can be attributed to the differences in image processing (12,20). Although adaptive thresholding has typically been used only for defining region volumes, in our work it was also applied for estimates of true activity. The validity of this approach still requires further evaluation. However, its use was encouraged by the accuracy obtained in the tests performed on the phantom experiment data. The adaptive threshold technique is easier than the meticulous drawing of manual region outlines slice by slice on CT scans—another common alternative for determining source volumes. Furthermore, tumors are sometimes not visible in CT images, especially nondiagnostic low-dose CT, such as the Infinia Hawkeye 4 SPECT/CT system.

**TABLE 3**  
Relative Absorbed Doses

Organ	Dose (mGy/MBq)
Kidneys	0.021 ± 0.007 (0.011–0.039)
Liver	0.012 ± 0.005 (0.005–0.028)
Spleen	0.030 ± 0.012 (0.005–0.057)
Thyroid	0.004 ± 0.001 (0.003–0.005)
Urinary bladder wall	0.014 ± 0.004 (0.008–0.024)

Data are average ± SD, followed by range in parentheses. Effective dose is 4.6 ± 1.1 mSv (2.7–6.4 mSv).

The average normal-organ relative absorbed doses estimated in this study were 0.021, 0.030, 0.014, and 0.012 mGy/MBq for the kidneys, spleen, urinary bladder, and liver, respectively. No statistical differences were noted in average organ absorbed doses when patients with and without pathologic uptake were considered separately. The <sup>99m</sup>Tc-HYNIC-TOC doses reported here are significantly lower than the previously reported <sup>111</sup>In-DTPA-octreotide dosimetry estimates of 0.41, 0.57, 0.20, and 0.10 mGy/MBq for the kidneys, spleen, bladder, and liver, respectively (21). Because <sup>111</sup>In injected activities are usually about 4–5 times lower than <sup>99m</sup>Tc activities, this translates to an approximately 4 times higher radiation dose to the kidneys with <sup>111</sup>In-DTPA-octreotide. The lower radiation dose associated with <sup>99m</sup>Tc-HYNIC-TOC imaging is particularly desirable for patients undergoing repeated scanning, as well as for younger patients.

In the only other published dosimetry study of <sup>99m</sup>Tc-HYNIC-TOC, by González-Vázquez et al., the reported doses for the kidneys, spleen, and liver were 0.029 ± 0.005, 0.033 ± 0.005, and 0.007 ± 0.001 mGy/MBq,

**TABLE 4**  
Tumor Masses, Tumor Doses, and Normal-Organ Doses for Patients with Pathologic Uptake

Patient no.	Tumors analyzed (n)	Tumor mass (g)*	Dose (mGy/MBq)			
			Tumors†	Kidneys	Liver	Spleen
1	3	139 (8–123)	0.041 (0.031–0.047)	0.024	0.014	0.030
3	7	85 (8–25)	0.004 (0.003–0.005)	0.012	0.011	0.015
10	1	17	0.005	0.023	0.015	0.039
17	2	1,455 (600–855)	0.004 (0.003–0.005)	0.023	0.014	0.037
19	3	249 (47–141)	0.024 (0.022–0.028)	0.023	0.012	0.034
21	1	23	0.013	0.033	0.014	0.025
22	1	122	0.018	ND	ND	ND
23	1	86	0.029	0.026	0.018	0.055
24	1	76	0.053	0.018	0.015	0.029
25	1	44	0.033	0.019	0.010	0.040
27	2	246 (70–176)	0.006 (0.004–0.007)	ND	ND	ND
28	1	7	0.016	0.013	0.010	0.024

\*When more than 1 lesion was analyzed, total mass is listed, followed by range in parentheses.

†When more than 1 lesion was analyzed, average dose is listed, followed by range in parentheses.

ND = not determined when region fell outside SPECT field of view.

respectively (10). Although the dose estimates in the 2 studies agree within the provided uncertainties, the mean doses estimated in the current study are approximately 30% less in the kidneys and 50% greater in the liver than the estimates of González-Vázquez et al. These differences could be due to the use of 2D imaging by González-Vázquez et al. versus the 3D imaging used in this work. It is widely recognized that there can be a large discrepancy between dose estimations using a 2D protocol and those using a 3D protocol (22). Significant errors in activity quantification based on a 2D processing method can be attributed to the inability to correctly account for attenuation, scatter, and overlapping source regions in planar images.

Using the patient-specific 3D dosimetry protocol outlined in this work, a large interpatient dose variation in normal organs and tumors was observed. The interpatient kidney dose ranged from 0.011 to 0.039 mGy/MBq, whereas the range of tumor doses varied from 0.003 to 0.053 mGy/MBq. Furthermore, the ratio of tumor-to-kidney dose ranged from 0.13 (patient 17) to 2.9 (patient 24). These different values reveal the importance of determining patient-specific dose estimates. The large variation in the tumor-to-kidney dose ratio among patients demonstrates how  $^{99m}\text{Tc}$ -HYNIC-TOC could possibly allow a physician to characterize therapy candidates and thus choose which cases are the more suitable for peptide receptor radionuclide therapy. Notably, the therapeutic agents of choice in peptide receptor radionuclide therapy are commonly  $^{90}\text{Y}$ -DOTATOC and  $^{177}\text{Lu}$ -DOTATATE, for which  $^{99m}\text{Tc}$ -HYNIC-TOC might not be an ideal candidate for accurate dose prediction, given the slightly different peptide structure and relatively short half-life of  $^{99m}\text{Tc}$ . Nonetheless, the information gained from a diagnostic scan with  $^{99m}\text{Tc}$ -HYNIC-TOC can still be useful for identifying patients with an increased somatostatin receptor subtype 2 expression and for recognizing those at increased risk of renal toxicity if treated with peptide receptor radionuclide therapy.

## CONCLUSION

This work outlines how hybrid planar/SPECT  $^{99m}\text{Tc}$ -HYNIC-TOC studies can provide clinicians not only with diagnostic (qualitative or semiquantitative) information but also with patient-specific quantitative parameters such as time-activity curves, absolute activity, and absorbed doses for tumors and normal organs. The large dose variations observed in this study demonstrate the significant impact that patient-specific considerations can have on treatment planning decisions. In the future, similar comprehensive analyses may serve to supplement the standard clinical examination of lesions overexpressing somatostatin receptor and may aid in the selection of patients for therapy through the accurate quantification of tumor and normal-organ uptake of radiolabeled somatostatin analogs.

## DISCLOSURE STATEMENT

The costs of publication of this article were defrayed in part by the payment of page charges. Therefore, and solely

to indicate this fact, this article is hereby marked "advertisement" in accordance with 18 USC section 1734.

## ACKNOWLEDGMENTS

This work was supported in part by a scholarship from the province of British Columbia through the Ministry of Advanced Education (Pacific Century Graduate Scholarship) and by a grant from the Polish Ministry of Education awarded to the Pomeranian Medical University, Department of Nuclear Medicine (PUM 12/10 PB). No other potential conflict of interest relevant to this article was reported.

## REFERENCES

1. Reubi J, Waser B, Schaer J, Laussie J. Somatostatin receptor sst1-sst5 expression in normal and neoplastic human tissues using receptor autoradiography with subtype-selective ligands. *Eur J Nucl Med*. 2001;28:836–846.
2. Krenning EP, Kwekkeboom DJ, Bakker WH, et al. Somatostatin receptor scintigraphy with [ $^{111}\text{In}$ -DTPA-d-Phe $^1$ ]- and [ $^{123}\text{I}$ -Tyr $^3$ ]-octreotide: The Rotterdam experience with more than 1000 patients. *Eur J Nucl Med Mol Imaging*. 1993;20:716–731.
3. Decristoforo C, Mather SJ, Cholewinski W, Donnemiller E, Riccabona G, Moncayo R.  $^{99m}\text{Tc}$ -EDDA/HYNIC-TOC: a new  $^{99m}\text{Tc}$ -labelled radiopharmaceutical for imaging somatostatin receptor-positive tumours; first clinical results and intra-patient comparison with  $^{111}\text{In}$ -labelled octreotide derivatives. *Eur J Nucl Med*. 2000;27:1318–1325.
4. Plachcińska A, Mikołajczak R, Maecke H, et al. Clinical usefulness of  $^{99m}\text{Tc}$ -EDDA/HYNIC-TOC scintigraphy in oncological diagnostics: a preliminary communication. *Eur J Nucl Med Mol Imaging*. 2003;30:1402–1406.
5. Czepczyński R, Parisella M, Kosowicz J, et al. Somatostatin receptor scintigraphy using  $^{99m}\text{Tc}$ -EDDA/HYNIC-TOC in patients with medullary thyroid carcinoma. *Eur J Nucl Med Mol Imaging*. 2007;34:1635–1645.
6. Gabriel M, Decristoforo C, Donnemiller E, et al. An inpatient comparison of  $^{99m}\text{Tc}$ -EDDA/HYNIC-TOC with  $^{111}\text{In}$ -DTPA-octreotide for diagnosis of somatostatin receptor-expressing tumors. *J Nucl Med*. 2003;44:708–716.
7. Maecke HR, Hofmann M, Haberkorn U.  $^{68}\text{Ga}$ -labeled peptides in tumor imaging. *J Nucl Med*. 2005;46(suppl):172S–178S.
8. Buchmann I, Henze M, Engelbrecht S, et al. Comparison of  $^{68}\text{Ga}$ -DOTATOC PET and  $^{111}\text{In}$ -DTPAOC (OctreoScan) SPECT in patients with neuroendocrine tumours. *Eur J Nucl Med Mol Imaging*. 2007;34:1617–1626.
9. Frilling A, Sotiropoulos GC, Radtke A, et al. The impact of  $^{68}\text{Ga}$ -DOTATOC positron emission tomography/computed tomography on the multimodal management of patients with neuroendocrine tumors. *Ann Surg*. 2010;252:850–856.
10. González-Vázquez A, Ferro-Flores G, Arteaga de Murphy C, Gutiérrez-García Z. Biokinetics and dosimetry in patients of  $^{99m}\text{Tc}$ -EDDA/HYNIC-Tyr $^3$ -octreotide prepared from lyophilized kits. *Appl Radiat Isot*. 2006;64:792–797.
11. Koral KF, Zasadny KR, Kessler ML, et al. CT-SPECT fusion plus conjugate views for determining dosimetry in iodine-131-monoclonal antibody therapy of lymphoma patients. *J Nucl Med*. 1994;35:1714–1720.
12. Daisne JF, Sibomana M, Bol A, Doumont T, Lonnet M, Grégoire V. Tri-dimensional automatic segmentation of PET volumes based on measured source-to-background ratios: influence of reconstruction algorithms. *Radiother Oncol*. 2003;69:247–250.
13. Siegel JA, Thomas SR, Stubbs JB, et al. MIRD pamphlet no. 16: techniques for quantitative radiopharmaceutical biodistribution data acquisition and analysis for use in human radiation dose estimates. *J Nucl Med*. 1999;40(suppl):37S–61S.
14. Shcherbinin S, Celler A, Belhocine T, Vanderwerf R, Driedger A. Accuracy of quantitative reconstructions in SPECT/CT imaging. *Phys Med Biol*. 2008;53:4595–4604.
15. Wells RG, Celler A, Harrop R. Analytical calculation of photon distributions in SPECT projections. *IEEE Trans Nucl Sci*. 1998;45:3202–3214.
16. Vandervoort E, Celler A, Wells G, Blinder S, Dixon K, Pang Y. Implementation of an analytically based scatter correction in SPECT reconstructions. *IEEE Trans Nucl Sci*. 2005;52:645–653.

17. Erdi YE, Wessels BW, Loew MH, Erdi AK. Threshold estimation in single photon emission computed tomography and planar imaging for clinical radioimmunotherapy. *Cancer Res.* 1995;55(23 suppl):5823s–5826s.
18. Bolch WE, Eckerman KF, Sgouros G, Thomas SR. MIRD pamphlet no. 21: a generalized schema for radiopharmaceutical dosimetry—standardization of nomenclature. *J Nucl Med.* 2009;50:477–484.
19. Stabin MG, Sparks RB, Crowe E. OLINDA/EXM: the second-generation personal computer software for internal dose assessment in nuclear medicine. *J Nucl Med.* 2005;46:1023–1027.
20. Veas H, Senthamizchelvan S, Miralbell R, Weber DC, Ratib O, Zaidi H. Assessment of various strategies for  $^{18}\text{F}$ -FET PET-guided delineation of target volumes in high-grade glioma patients. *Eur J Nucl Med Mol Imaging.* 2009;36:182–193.
21. Radiation dose to patients from radiopharmaceuticals (addendum to ICRP publication 53): ICRP publication 80. *Ann ICRP.* 1998;28.
22. He B, Wahl RL, Du Y, et al. Comparison of residence time estimation methods for radioimmunotherapy dosimetry and treatment planning: Monte Carlo simulation studies. *IEEE Trans Med Imaging.* 2008;27:521–530.